

Designing Supramolecular Liquid-Crystalline Hybrids from Pyrenyl-Containing Dendrimers and Arene Ruthenium Metallacycles

Anaïs Pitto-Barry,[†] Nicolas P. E. Barry,[†] Virginie Russo,[†] Benoît Heinrich,[‡] Bertrand Donnio,^{*,‡,§} Bruno Therrien,^{*,†} and Robert Deschenaux^{*,†}

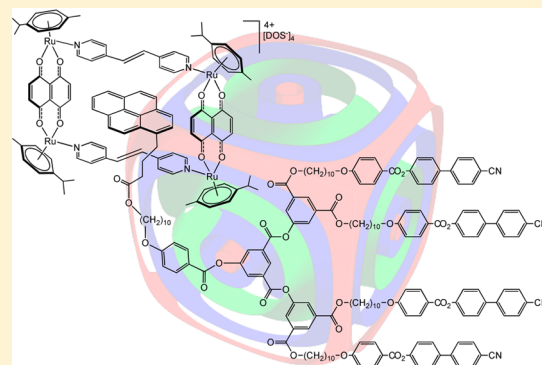
[†]Institut de Chimie, Université de Neuchâtel, Avenue de Bellevaux 51, 2000 Neuchâtel, Switzerland

[‡]Institut de Physique et Chimie des Matériaux de Strasbourg (IPCMS), UMR 7504, CNRS—Université de Strasbourg, 23 rue du Loess, BP43, 67034 Strasbourg cedex 2, France

[§]Complex Assemblies of Soft Matter Laboratory (COMPASS), UMI 3254, CNRS/Solvay/University of Pennsylvania, CRTB, 350 George Patterson Boulevard, Bristol, Pennsylvania 19007, United States

S Supporting Information

ABSTRACT: The association of the arene ruthenium metallacycle $[\text{Ru}_4(p\text{-cymene})_4(\text{bpe})_2(\text{donq})_2][\text{DOS}]_4$ ($\text{bpe} = 1,2\text{-bis}(4\text{-pyridyl})\text{-ethylene}$, $\text{donq} = 5,8\text{-dioxydo-1,4-naphtoquinonato}$, DOS = dodecyl sulfate) with pyrenyl-functionalized poly(arylester) dendrimers bearing cyanobiphenyl end-groups is reported. The supramolecular dendritic systems display mesomorphic properties as revealed by polarized optical microscopy, differential scanning calorimetry and small-angle X-ray scattering measurements. The multicomponent nature of the dendrimers and of the corresponding host–guest supramolecules (i.e., end-group mesogens, dendritic core, pyrene unit, aliphatic spacers, and metallacycle) leads to the formation of highly segregated mesophases with a complex multilayered structure due to the tendency of the various constitutive building-blocks to separate in different organized zones. The pyrenyl dendrimers exhibit a multilayered smectic A-like phase, thereafter referred to as LamSmA phase to emphasize this unaccustomed morphology. As for the corresponding Ru_4 –metallacycle adducts, they self-organize into a multicontinuous thermotropic cubic phase with the $I\bar{m}\bar{3}m$ space group symmetry. This represents a unique example of liquid-crystalline behavior observed for such large and complex supramolecular host–guest assemblies. Models of their supramolecular organizations within both mesophases are proposed.



INTRODUCTION

The development of composite materials has recently opened up new avenues for the design of highly innovative materials. Their properties and spectrum of applications span across electronic circuitry, nanosmart materials, and nanocatalysts. Metallomesogens (metal-containing liquid crystals) combine the properties of both the metal ion (e.g., optical, electronic, magnetic, catalytic properties, coordination geometry) and the mesogenic part (e.g., structure-dependent organization, fluidity, stimuli-responsive behavior). They offer a unique platform for synthesizing compounds with magnetic, optical, and electro-optical properties. Incorporation of metallic ions in liquid-crystalline (LC) materials extends further possible novel intermolecular interactions such as metal–metal (metallophilic) and metal–ligand interactions, which can have important consequences on the physical properties (e.g., amplification or emergence of new properties) and on the self-assembling abilities.¹ A wide variety of metallomesogens has been generated to date using concepts based on coordination, organometallic and supramolecular chemistry. Such a diversity of structures embraces from simple to very sophisticated

molecular systems, including one-metal center systems,² metal dimer molecules,³ metal–metal bonded molecules,⁴ metallocenes, buckyferrocenes,⁵ metallohelicates,⁶ metallacrowns,⁷ customesogens,⁸ heteropolymetallic metallomesogens,⁹ metalomesogenic polymers, and two-dimensional networks.¹⁰ Mesogens can also be introduced in metal-containing liquid crystals as counterions.¹¹ Incorporation of metal-containing building-blocks in liquid-crystalline molecules usually results in substantial modifications of the initial mesomorphic properties of the ligands (e.g., changes of mesophase symmetry, thermodynamic stability, transition temperatures). When these metallic blocks are much larger than the mean size of the mesogenic part, mesomorphism can even be suppressed. However, their incorporation into LC phases has been successfully achieved through the use of voluminous mesomorphic dendritic systems,¹² and beautiful examples of LC catenanes¹³ and rotaxanes¹⁴ among other systems^{15,16} can be found in the literature.

Received: October 8, 2014

Published: November 24, 2014

Herein, we report the synthesis, properties, and supramolecular organization of the first members of a new family of liquid-crystalline host–guest complexes based on an organometallic Ru_4 cage (host) and liquid-crystalline dendrimers (guests). The synthesis of the third-generation (\mathbf{P}_3) poly(arylester) dendrimer containing cyanobiphenyl mesogens functionalized with a pyrenyl unit is reported (Supporting Information). The preparation of the second-generation dendrimer \mathbf{P}_2 was already described (Supporting Information). The synthesis of the tetranuclear arene ruthenium salt $[\text{Ru}_4(p\text{-cymene})_4(\text{bpe})_2(\text{donq})_2][\text{DOS}]_4$ ($\text{bpe} = 1,2\text{-bis}(4\text{-pyridyl})\text{-ethylene}$; $\text{donq} = 5,8\text{-dioxydo-1,4-naphthoquinonato}$; $\text{DOS} = \text{dodecyl sulfate}$), abbreviated as $[\mathbf{1}][\text{DOS}]_4$, is also reported. The cationic metallacycle $[\mathbf{1}]^{4+}$ was previously isolated as its triflate salt,¹⁷ but no liquid-crystalline behavior was observed when \mathbf{P}_2 or \mathbf{P}_3 was included in $[\mathbf{1}][\text{CF}_3\text{SO}_3]_4$. Clearly, the choice of the counterion is crucial for the design of metallomesogens.^{1,18} Therefore, in this study, we used the dodecyl sulfate anion (DOS), a long and flexible ionic surfactant, which usually contributes efficiently to the decrease of the melting points of the corresponding salts.¹⁸

The liquid-crystalline properties and supramolecular organization of the pyrenyl-based dendrimers \mathbf{P}_n and their inclusion complexes $[\mathbf{P}_n \subset \mathbf{1}][\text{DOS}]_4$ were investigated by polarized optical microscopy (POM), differential scanning calorimetry (DSC) and small-angle X-ray scattering (SAXS). The dendrimers showed a multilayered smectic A-like phase (referred thereafter to as LamSmA) in agreement with their multiblock architecture and the presence of peripheral calamitic mesogens. The $[\mathbf{P}_n \subset \mathbf{1}][\text{DOS}]_4$ revealed an unexpected supramolecular organization into a multicontinuous cubic phase.

RESULTS AND DISCUSSION

Design. The assembly of $\mathbf{1}$ with \mathbf{P}_n is based on the ability of the cage to interact with the planar π -conjugated pyrenyl moiety via hydrophobic and π – π interactions.¹⁷ Second- and third-generation dendrimers were selected as liquid-crystalline promoters to thwart the size of the cage. Among the tetra-, hexa- and octacationic arene ruthenium metallacycles already known,¹⁹ we selected the species with the lowest global charge. This choice was motivated by previous experiments in which anticancer drug candidates composed of liquid-crystalline dendrimers included in a hexacationic arene ruthenium metallaprism, $[\text{Ru}_6(p\text{-cymene})_6(\text{tpt})_2(\text{donq})_3]^{6+}$ ($\text{tpt} = 2,4,6\text{-tri(pyridine-4-yl)-1,3,5-triazine}$) were found to be nonmesomorphic.²⁰

Synthesis of the Dendrimers. Second- and third-generation pyrenyl poly(arylester) dendrimers, \mathbf{P}_2 and \mathbf{P}_3 , respectively (Figure 1), were synthesized by two successive esterification reactions [N,N' -dicyclohexylcarbodiimide (DCC), 4-(dimethylamino)pyridinium *para*-toluenesulfonate (DPTS)].²¹ The first coupling between 1-pyrenebutyric acid and 4-((10-hydroxydecyl)oxy)benzoic acid,²² which gave a new pyrene derivative was subsequently esterified with the corresponding second- and third-generation phenol-based dendrons²² (Scheme S1). Dendrimers \mathbf{P}_2 and \mathbf{P}_3 were characterized by ^1H , ^{13}C NMR, UV-visible and IR spectroscopies, elemental analyzes and ESI-mass spectrometry (Supporting Information).

Synthesis of the Arene Ruthenium Metallacycle. The tetranuclear arene ruthenium complex $[\text{Ru}_4(p\text{-cymene})_4(\text{bpe})_2(\text{donq})_2][\text{DOS}]_4$ ($[\mathbf{1}][\text{DOS}]_4$) was prepared

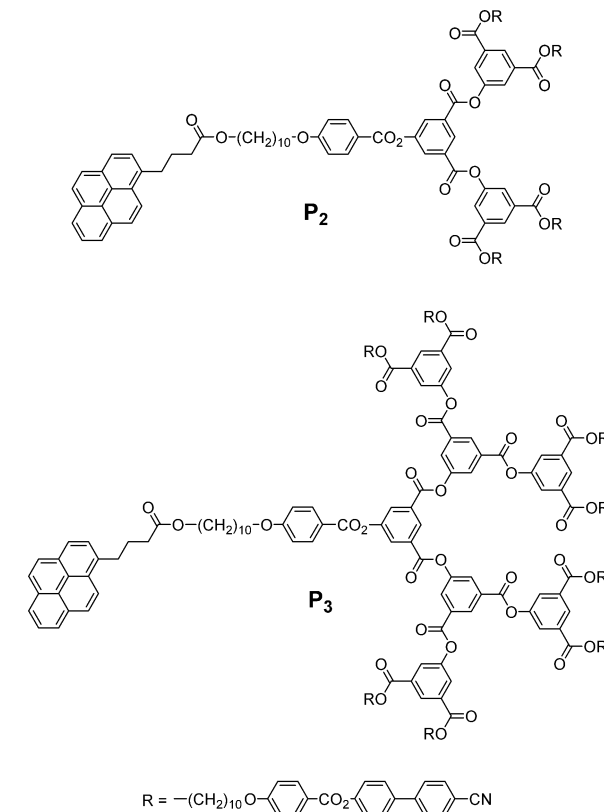
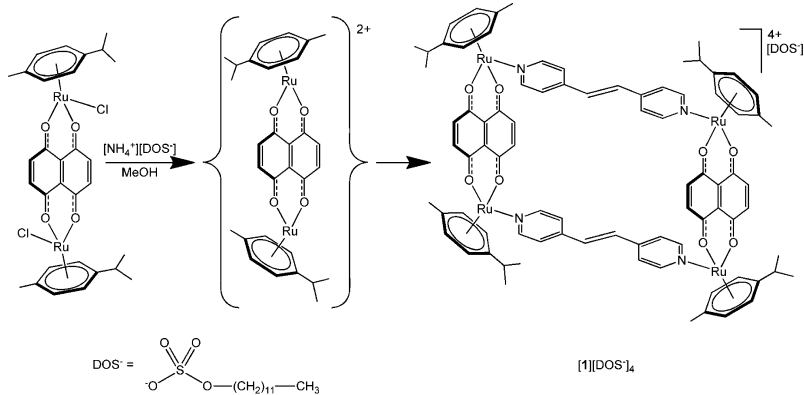


Figure 1. Structures of the second- and third-generation dendrimers \mathbf{P}_2 and \mathbf{P}_3 .

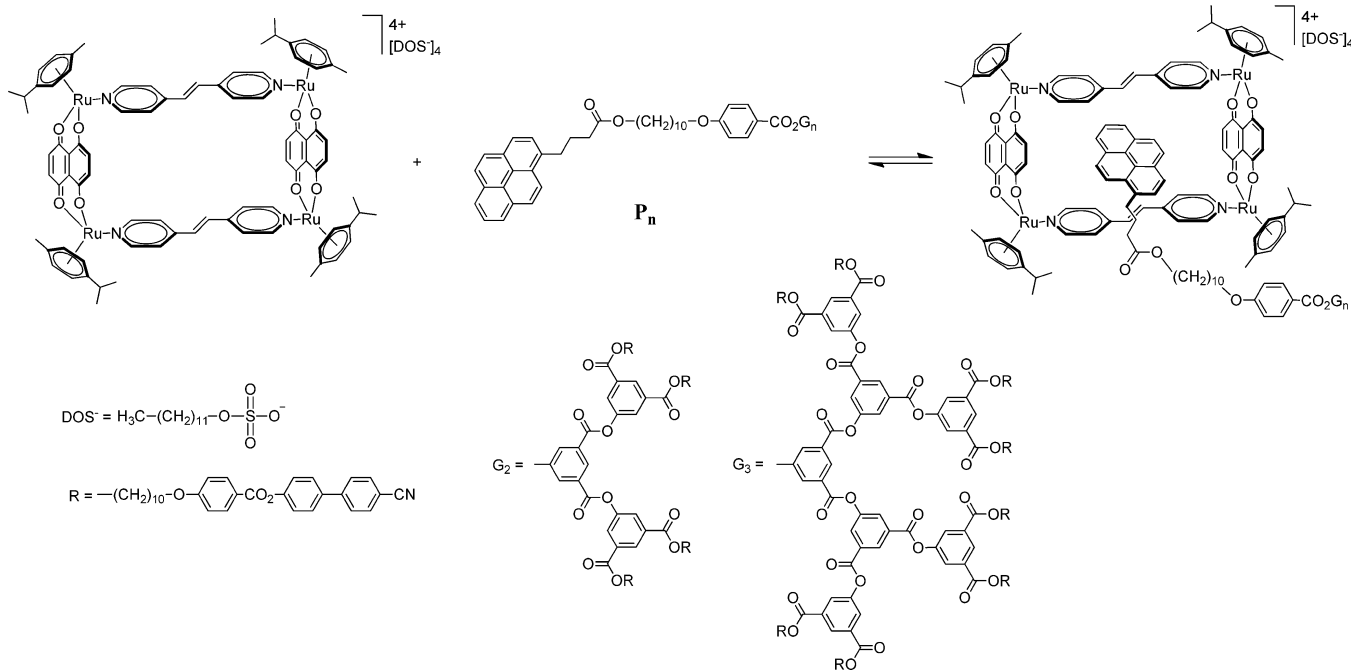
in methanol from the dinuclear complex $[\text{Ru}_2(p\text{-cymene})_2(\text{donq})_2\text{Cl}_2]$ and the bidentate ligand bpe in the presence of ammonium dodecyl sulfate in good yield (76%) following a procedure already used to obtain this cationic rectangle as a triflate salt (Scheme 1).¹⁷ Here, the ammonium cation is used as a halide scavenger; the dicationic intermediate is not isolated.

The ^1H NMR spectrum (CD_2Cl_2 , 25 °C) of $[\mathbf{1}][\text{DOS}]_4$ is in agreement with the spectrum of its triflate analogue $[\mathbf{1}]\text{-}[\text{triflate}]_4$.¹⁷ The signals of the bpe protons are shifted upfield as compared to those of the free bpe. The signal of the 5,8-dioxydo-1,4-naphthoquinonato bridging ligands is shifted down-field as compared to the parent complex $[\text{Ru}_2(p\text{-cymene})_2(\text{donq})_2\text{Cl}_2]$, while the methyl, isopropyl and phenyl resonances of the *p*-cymene protons are almost unchanged. The signals of the aliphatic protons of the dodecyl sulfate counterion are well resolved and found at 3.76, 1.46–1.34 and 0.72 ppm, respectively. The ^{13}C NMR spectrum of the salt was recorded in CD_2Cl_2 at 21 °C and fully attributed (Supporting Information). Metallacycle $[\mathbf{1}][\text{DOS}]_4$ is not stable under ESI-mass spectrometry but the fragmentation peak corresponding to $[\text{Ru}_2(p\text{-cymene})_2(\text{donq}) + \text{bpe} + (\text{DOS})]^+$ is found at 1107.27. This fragmentation is typical of arene ruthenium metallacycles.²³ Despite being unstable under ESI-mass spectrometry, such metallacycles have been found to be extremely stable in solution and even at elevated temperature.²³ The purity of $[\mathbf{1}][\text{DOS}]_4$ was confirmed by elemental analysis (Supporting Information).

Synthesis of the Supramolecular Assemblies. A solution of one equivalent of both \mathbf{P}_n and $[\mathbf{1}][\text{DOS}]_4$ was stirred during 2 days in CH_2Cl_2 at room temperature (Scheme 2). Then, the solvent was removed by slow evaporation. The compounds were dried for several days. Elemental analysis

Scheme 1. Synthesis of the Arene Ruthenium Metallacycle Isolated As Its Dodecyl Sulfate Salt, $[1][\text{DOS}]_4$ ^a

^aConditions: MeOH, NH_4DOS , bpe, 60 °C, 24 h.

Scheme 2. Synthesis of the $[\text{P}_n \subset 1][\text{DOS}]_4$ Assemblies^a

^aConditions: CH_2Cl_2 , rt, 2 days.

confirmed the purity of the systems and the absence of residual solvent (Supporting Information). Direct grinding of one equivalent of $[1][\text{DOS}]_4$ with one equivalent of P_2 or P_3 did not lead to materials displaying liquid-crystalline properties. In this case, heterogeneous black areas of nonmelted metallacycle with zones of melted dendrimer (in the mesophase) were observed by POM. This observation indicates that the interactions in solution between the pyrenyl part and the metallacycle are crucial for the formation of homogeneous liquid-crystalline systems.

Solution Studies. The ^1H NMR spectra of the two systems show differences with the spectra of previously reported $[\text{pyrene} \subset 1]^{4+}$ host–guest systems.²⁴ Indeed, in such systems, broadening and important chemical shifts of the signals of the bpe and donq protons were observed, while in the systems described herein, all the signals remain narrow and well resolved (Supporting Information). However, slight chemical shifts of the donq and bpe proton resonances are observed,

suggesting an in-cavity interaction between the pyrenyl part of the functionalized dendrimer and the metallacycle. Diffusion-ordered NMR spectroscopy (DOSY) experiments were performed to study the nature of the interactions between P_2 or P_3 and $[1]^{4+}$ and confirmed that an interaction occurs but without complete encapsulation of the pyrene into the cavity of the metallacycle in solution (Figure 2). A decrease of $\log D$ can be observed for each part of the assembly when they are mixed together in solution, which indicates strong host–guest interactions in the order of $60\,000\,\text{M}^{-1}$.²⁴ However, the fact that the signals associated with P_3 and $[1]^{4+}$ diffuse at different rates suggests a relatively fast in- and out-of-cavity interaction in solution (CD_2Cl_2 , 21 °C).

The ^{13}C NMR spectra of the two systems were recorded in CD_2Cl_2 at 21 °C and fully attributed (Supporting Information). The ESI-mass spectra of the two associated systems display the same fragmentation pattern $[\text{Ru}_2(p\text{-cym})_2](\text{donq}) + \text{bpe} + (\text{DOS})^+$ at 1107.27 than the spectrum of $[1][\text{DOS}]_4$. The

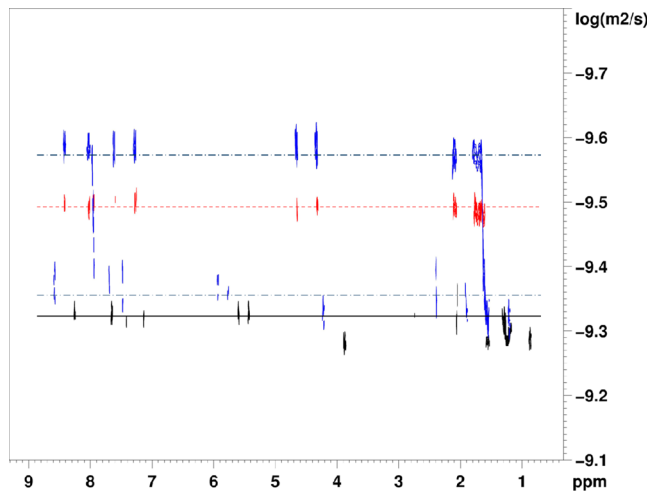


Figure 2. DOSY NMR spectra of \mathbf{P}_3 (red), $[1]^{4+}$ (black) and the corresponding associated system (blue) in CD_2Cl_2 at 21°C .

compounds were also characterized by UV-vis and IR spectroscopy (Supporting Information).

Liquid-Crystalline Properties and Supramolecular Organization of Dendrimers \mathbf{P}_2 and \mathbf{P}_3 . The two pyrenyl-functionalized dendrimers \mathbf{P}_n led to the formation of a broad SmA-like phase above their glass transition temperatures (T_g) (Table 1). The mesophases were partly identified by POM

Table 1. Phase-Transition Temperatures of Dendrimers \mathbf{P}_2 and \mathbf{P}_3

compound	T_g^a	transition ^b	T_i^a	ΔH (kJ·mol ⁻¹)
\mathbf{P}_2	33	LamSmA → I	165	9.4
\mathbf{P}_3	60	LamSmA → I	219	39.6

^a T_g = glass transition temperature, T_i = isotropization temperature. ^bLamSmA = multilayered smectic A-like phase (see text), I = isotropic liquid. Temperatures (in $^\circ\text{C}$) are given as the onset of the peak obtained during the second heating run; the T_g were determined during the first cooling cycle (rate: $10^\circ\text{C}\cdot\text{min}^{-1}$).

from the formation of typical focal-fan conic textures and homeotropic areas (Figure 3), indicative of uniltted lamellae. The increase of the clearing temperature is concomitant with the increase of the dendritic generation as usually observed with this family of dendrimers.^{16,25} This trend confirms that the stability of the mesophases increases with the number of mesogens.

The structures of the mesophases displayed by \mathbf{P}_2 and \mathbf{P}_3 were studied by SAXS. The samples were measured from room temperature up to 160°C (\mathbf{P}_2) and 200°C (\mathbf{P}_3), respectively. Analysis of the diffractograms (Figures 4, 5 and S6) confirmed that both dendrimers \mathbf{P}_2 and \mathbf{P}_3 display a single smectic-like phase, in agreement with POM observations.

For \mathbf{P}_2 , two sharp low-intensity reflections in a 1:2 ratio were detected in the small-angle range at 53.8 and 26.7 \AA [Figure 4, reflections indexed as (001) and (002), respectively], confirming the layered structure of the mesophase with a periodicity of $d = 53.8\text{ \AA}$. In addition, were also observed the classical wide-angle broad scattering with a maximum at ca. 4.4 – 4.6 \AA originating from the overlapping distances between molten aliphatic chains (h_{ch}), dendritic core (h_{dend}) and mesogens (h_{mes}), respectively (Figure 4, $h = h_{\text{ch}} + h_{\text{dend}} + h_{\text{mes}}$), and another large, small-angle diffusion with a maximum

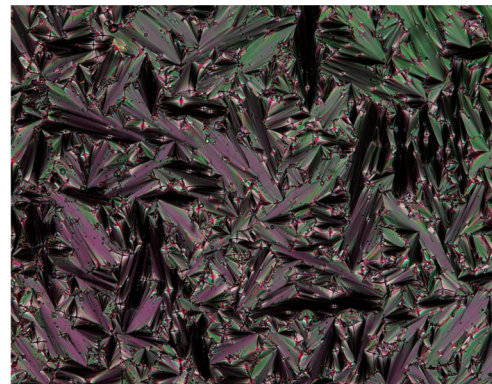
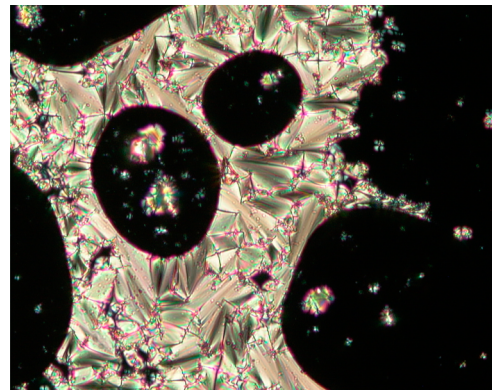


Figure 3. Thermal-polarized optical micrographs of the focal-conic fan textures of the SmA-like phase displayed by \mathbf{P}_2 , at $T = 150^\circ\text{C}$ (top) and \mathbf{P}_3 , at $T = 145^\circ\text{C}$ (bottom) upon cooling the samples from the isotropic liquid.

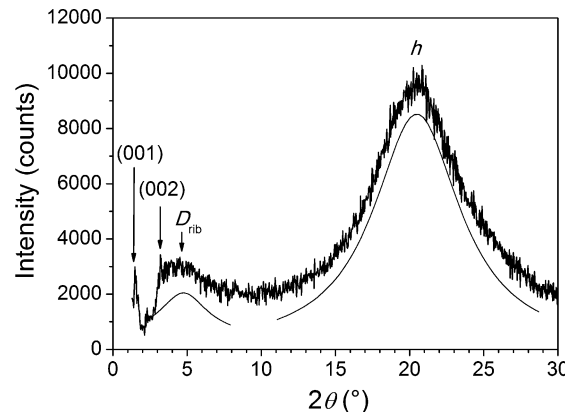


Figure 4. Representative SAXS patterns of \mathbf{P}_2 at $T = 80^\circ\text{C}$.

at ca. 21 – 22 \AA which was attributed to some molecular correlations caused by specific short-range ordering of the pyrene segments (labeled as D_{rib} , Figures 4 and S6) within the layers (see below).

Above 40 – 50°C , the X-ray diffraction patterns of \mathbf{P}_3 (Figure 5) display four sharp small-angle reflections in the 1:2:3:4 ratio [at 55.5 , 27.5 , 18.4 , and 13.8 \AA , indexed as (00*l*) reflections and $l = 1$ – 4], which also attest for the formation of a lamellar phase with a periodicity of $d = 55.2\text{ \AA}$ ($d = \sum l \cdot d_{00l} / N_l$, where N_l is the number of 00*l* reflections). As for \mathbf{P}_2 , similar broad scattering signals ($h = 4.4$ – 4.6 \AA and $D = 25$ – 26 \AA , the latter slightly shifted to smaller angles) are also observed for this compound (Figures 5 and S6). In addition, one can also recognize a broad

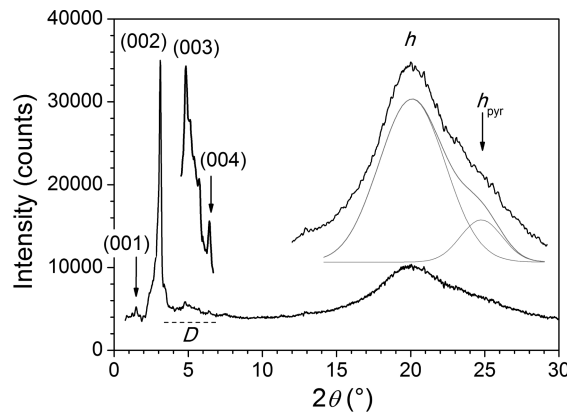


Figure 5. Representative SAXS patterns of \mathbf{P}_3 at $T = 80\text{ }^\circ\text{C}$.

signal at ca. 3.5 \AA , h_{pyr} , attributed to π stacking of pyrenyl cores (see below).

X-ray patterns thus unambiguously confirm the formation of a smectic-like phase for \mathbf{P}_2 and \mathbf{P}_3 . As the generation is increased, the presence of up to four thin reflections indicates good molecular segregation (sharp interfaces) of the different constitutive blocks of the dendrimers. Thus, the mesogenic groups connected at the periphery of the dendrimers act as classical calamitic smectogens, and therefore direct the formation of a lamellar phase, similarly to other structurally related dendrimers.^{12,16} The specific multiblock molecular architecture of \mathbf{P}_n dendrimers further imposes the segregation between the cyanobiphenyl units and the appended pyrenes with the dendritic cores and aliphatic spacers.¹² This is clearly evidenced by the abnormal intensity profile distribution of the low-angle reflections series, with a relatively exhausted first-order (001) reflection and an enhanced second-order (002) reflection revealing the periodic alternation of several high-electronic density sublayers associated with the mesogenic end-groups and the dendritic scaffold, respectively, with low-electronic density sublayers associated with the molten aliphatic

spacers (Figures 4, 5 and S6). The observation of the characteristic optical texture of the SmA confirms this organization for the mesogens, and the disordered liquid-like state of the dendritic cores within the median sublayer. Apart from the formation of the lamellae, a further segregation process occurs inside the mesogen sublayers between the cyanobiphenyl mesogens and the pyrene groups, as revealed by the appearance of the additional small-angle scattering signal (labeled D_{rib} and D , for \mathbf{P}_2 and \mathbf{P}_3 , respectively). The long spacer between the pyrene moiety and the dendron allows the former to reach the sublayer formed by the mesogenic groups. The relative high intensity of this signal arises from the insertion of a fraction of the spacer segments in the mesogenic sublayer, due to the different end-group lengths (ca. 18 and 8 \AA for mesogen and pyrene, respectively). However, the patterning of the layer perforation remains short-range, as deduced from the broad signal shape (correlation lengths from Scherrer formula are about 25 and 50 \AA for \mathbf{P}_2 and \mathbf{P}_3). The peak location $D_{\text{rib}} \approx 21\text{ \AA}$ for the lower generation is compatible with the segregation of pyrenes and spacer segments in continuous ribbons alternating with strips formed by the 4 times more abundant cyanobiphenyl mesogens fraction (Figure 6). The continuity of the ribbons can however not be maintained in the higher generation compound because of the further dilution of the pyrene moieties, as confirmed by the maximum shift to $D \approx 26\text{ \AA}$ in \mathbf{P}_3 : pyrenes and spacer segments then segregate into islands positioned at the nodes of a loose pseudohexagonal lattice. The average aggregation number of associated pyrene groups can be estimated from D by using an approach detailed elsewhere,²⁶ giving $3\text{--}4$ units per island (Figure 6). The patterning of the layer optimizes the separation in space of incompatible mesogens and incorporated spacer segments, but still interferes with the parallel alignment of the mesogens and with the cohesion of the layer. The reduced hindrance with the smaller islands indeed constitutes one feature explaining the higher isotropization temperature and the larger isotropization enthalpy per mesogen of \mathbf{P}_3 .

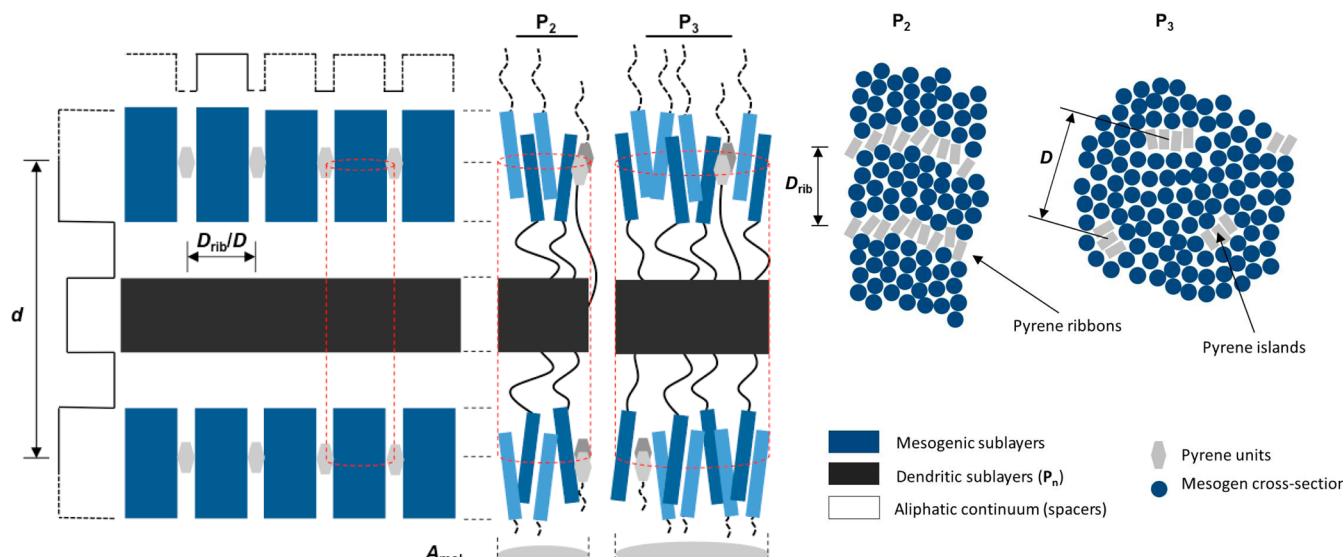


Figure 6. Postulated schematic supramolecular organization of \mathbf{P}_2 and \mathbf{P}_3 within the LamSmA phase; the side view (left) shows the alternation of the different sublayers, while the top view (right) reveals the local perforations of the mesogenic outerlayers. Profiles (far left): electronic density modulations in the direction perpendicular to the layers (d) and within the layers (D_{rib}/D).

For a more detailed understanding of the mesophase structure, the lamellar packing can be further characterized by the molecular area, A_{mol} , ratio of the molecular volume, V_{mol} , and layer spacing, d . For \mathbf{P}_2 and \mathbf{P}_3 , the molecular volumes are estimated to be around ca. 4970 and 9240 Å³ respectively (considering a density close to 0.95 at 80 °C) and the molecular areas ca. 92 and 167 Å², respectively, quasi-doubling from \mathbf{P}_2 to \mathbf{P}_3 in consistency with the doubling of the number of peripheral cyanobiphenyl units (4 → 8) and generation (2 → 3). These values and the quasi-invariance of the lamellar periodicities ($d = 53.8$ Å versus $d = 55.2$ Å), despite the doubling of the volume with increasing generation, is indicative of the molecular expansion within the layers and a similar packing mode for both systems, which evidently is imposed by the unfolded dendritic core. These A_{mol} values are nevertheless significantly smaller than the overall cross section of the mesogen end-groups (estimated to be 115 and 205 Å² from reference volumetric data).²⁷ Such a discrepancy is commonly encountered for mesogens with one end devoid of terminal chain, as mesogens attached to segments from neighboring sublayers can either associate tip-to-tip into dimers or interdigitate over their whole length.²⁷ Depending upon the statistical proportion of dimers, the mesogens can either form monolayer, bilayer, or partial-bilayer arrangements (Figure S7).²⁸ This dimer proportion lays here at 35%, as typically found for cyanobiphenyl compounds.²⁸

On the basis of these calculations and the relative intensities of the reflections, the structure of the lamellar phase consists of a central sublayer containing the expanded, disordered dendritic cores, separated from the perforated mesogenic layers (from the pyrenes and intercalated chain fractions) by the aliphatic continuum (made from the spacers) (Figure 6). In both cases, the dendrimers logically adopt an elongated pseudo-“cylindrical” conformation with the peripheral mesogens and pyrenes distributed homogeneously on either side of the dendritic scaffold, and separated by the aliphatic spacers. Such a highly segregated molecular conformation is in agreement with the fundamental lamellar periodicities. Since this structure differs substantially from a classical SmA phase, this phase was preferentially labeled as LamSmA to highlight its particular multilayer structure. Such lamellar mesophases with sublayers patterned by ribbons (\mathbf{P}_2) or islands (\mathbf{P}_3) better accommodate the multisegregated architecture. Despite of being rarely reported, they have nevertheless been previously observed in block copolymers and small molecules with rodlike mesogens bearing side-on substituents.²⁹

Liquid-Crystalline Properties and Supramolecular Organization of $[\mathbf{P}_2 \subset \mathbf{1}][\text{DOS}]_4$ and $[\mathbf{P}_3 \subset \mathbf{1}][\text{DOS}]_4$ Host–Guest Complexes. In their molten state, none of the complexes appeared birefringent when observed by POM, but only the formation of highly viscous, large dark, texture-less areas were detected when pressure was applied on the glass slide. Above 100 °C, degradation was observed, likely resulting from the irreversible dissociation of the supramolecular species, a situation often encountered in liquid-crystalline inclusion complexes.³⁰ The structure of their mesophases below 100 °C was eventually deduced by SAXS, namely a thermotropic cubic phase (with the $I\bar{m}\bar{3}m$ space group symmetry), from room-temperature up to ca. 100 °C for $[\mathbf{P}_2 \subset \mathbf{1}][\text{DOS}]_4$, and between 50 °C and ca. 100 °C for $[\mathbf{P}_3 \subset \mathbf{1}][\text{DOS}]_4$ (an amorphous state is observed below 50 °C). No practical information could be deduced from the DSC experiments since

a dissociation/decomposition of the samples occurs before the clearing point was reached.

Both systems exhibit similar X-ray patterns (Figures 7 and 8) with several small-angle reflections and two large diffuse

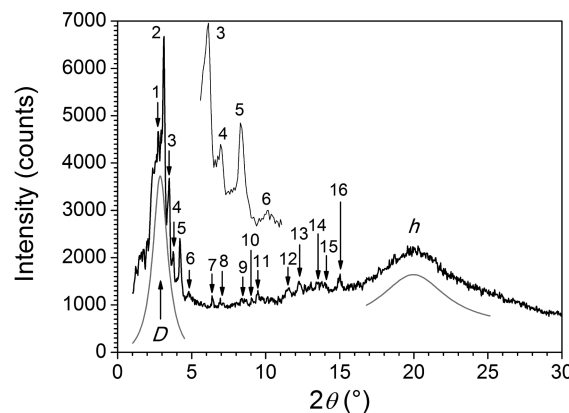


Figure 7. Representative SAXS patterns of $[\mathbf{P}_3 \subset \mathbf{1}][\text{DOS}]_4$ at $T = 80$ °C.

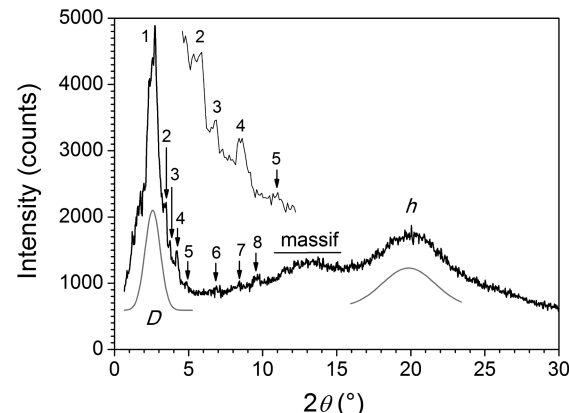


Figure 8. Representative SAXS patterns of $[\mathbf{P}_2 \subset \mathbf{1}][\text{DOS}]_4$ at $T = 80$ °C.

scatterings, one at wide-angle evidencing the molten state of the chains, dendritic cores and mesogens ($h = 4.4$ –4.5 Å), and another one in the small-angle range (at ca. 32–33 Å), which is attributed to short-range correlated structures emerging from the distribution of different zones. Indeed, this periodicity, D , is related to the ionic lattice and arises from the electron-rich metallacycle, and from the segregation patterning with the cyanobiphenyl end-group (presumed to be similar to the perforations in the LamSmA phases for the \mathbf{P}_n guests).

The SAXS pattern of $[\mathbf{P}_3 \subset \mathbf{1}][\text{DOS}]_4$ reveals 16 sharp, small-angle reflections (Figure 7, Table S1) with reciprocal d -spacings in ratios theoretically compatible with both primitive (P) and body-centered (I) space groups, while it unambiguously excludes a face-centered cfc network (F). The SAXS pattern of $[\mathbf{P}_2 \subset \mathbf{1}][\text{DOS}]_4$ recorded at 80 °C (Figure 8, Table S2) is similar, but exhibits fewer reflections, with a series of 8 defined peaks, and a massif of unresolved wide-angle signals. The lower number of reflections a priori precludes a definitive phase assignment for $[\mathbf{P}_2 \subset \mathbf{1}][\text{DOS}]_4$, but the similarity between the SAXS patterns of both host–guest complexes suggests that they both self-organize in the same type of cubic phase.

Although the diffraction patterns were theoretically compatible with a primitive lattice (P) as previously observed in cubic liquid-crystalline phases,³¹ the allowed groups ($Pm\bar{3}$, $Pn\bar{3}$, $Pm\bar{3}m$, $Pm\bar{3}n$, $Pn\bar{3}n$ and $Pn\bar{3}m$) leave the absence of too many reflections unexplained and can be safely excluded. Only two centered space groups can thus be considered, $Im\bar{3}$ and $Im\bar{3}m$, since the groups reflection conditions are satisfied.³² Aggregation into the highest symmetry is generally admitted, and, accordingly, the $Im\bar{3}m$ space group (N° 229) was retained.³² Therefore, the symmetry of the cubic phases of the $[P_n \subset 1][DOS]_4$ host–guest systems is characterized by a body-centered cubic network (I), with lattice parameters $a = 85.4$ and 86.8 Å for $[P_2 \subset 1][DOS]_4$ and $[P_3 \subset 1][DOS]_4$, respectively (Tables S1 and S2). On the basis of the partial volume of $[1][DOS]_4$ estimated to 3600 Å³, and thus considering approximated molecular volumes (V_{mol}) of 8600 and $12\,800$ Å³ (density, $\rho \approx 1.05$ g·cm⁻³ at 80 °C) for both complexes, each cubic unit cell contains ca. 72 ± 2 and 50 ± 2 supramolecules, respectively. These large aggregation numbers combined with the shape of the SAXS patterns agree with a highly segregated, multicontinuous structure (see below). It is moreover unusual that the observable reflections are so numerous and propagate so far in the midangle range for thermotropic cubic phases (Tables S1 and S2). This feature proves the high degree of nanosegregation between incompatible segments, as they are confined in domains separated by sharp interfaces. The insertion of the metallacycle DOS salt certainly preserves the differentiation of dendritic and mesogen moieties inherited from P_2 and P_3 pyrenyl dendrimers (see below), but concomitantly imposes intricate and sterically constrained arrangements of the corresponding segregated domains. Nearly the same intricate multicontinuous structure is obtained for both host–guest systems, with even an extension of the reflection series to larger Miller indices for the higher-generation dendrimer, following the trend observed in the lamellar phase of the pyrenyl dendrimers.

Molecular organizations proposed for previous thermotropic multicontinuous cubic phases are based on minimal surfaces of type P and G, in accordance with the observed $Im\bar{3}m$ and $Ia\bar{3}d$ symmetries.^{33,34} As seen above, the $Ia\bar{3}d$ symmetry, and therefore the G minimal surfaces, are here clearly excluded [presence of the (310), (222), (330)/(441) reflections being incompatible with this group], and the $Im\bar{3}m$ symmetry confirmed. Remarkably, some authorized reflections are missing in the series, especially those at lowest angles [i.e., (110), (200), (211)]. Although the overlapping with the intense small-angle scattering may partially hinders the detection of these reflections, their absence (or weakness) follows an intensity modulation that goes through a maximum for reflections (310) and (222) in the generation 3, and for reflection (220) in the generation 2. As a regular decrease is commonly observed for bicontinuous phases,³⁴ this modulation is a further proof for a more complex multicontinuous structure.^{35,36}

The emergence of the three-dimensional structure evidently follows the expansion of the mesogen and aliphatic sublayers by the metallacycle DOS salt, which creates discrepancies with the molecular area of the dendritic-containing sublayer. Such a distortion of the layering is counter-balanced by the curvature at both interfaces (i.e., mesogenic/aliphatic and dendritic/aliphatic interfaces) and results in the fusion of the lamellae into intricate, intermingled three-dimensional networks (interwoven “labyrinths” in Figure 9 and S8). Tentatively, a more comprehensive description of the organization is proposed

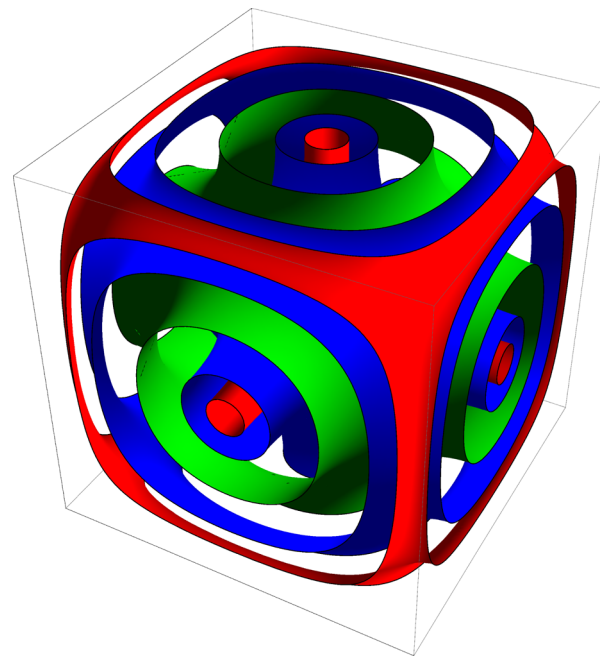


Figure 9. Schematic representation of the multicontinuous cubic structure (surface foliation model^{34,37,38}) for the host–guest complex $[P_2 \subset 1][DOS]_4$: Representation of the different intermediate interfaces β (red for the aliphatic/dendritic interfaces, $|\beta| = 1.89$; blue for the mesogen/aliphatic interfaces, $|\beta| = 1.44$) on both sides of the isosurface of zero-mean curvature ($\beta = 0$, green).

through the adaptation of a multicontinuous structural model, already validated for some thermotropic $Im\bar{3}m$ systems.³⁴ This model is based on the foliation of the lattice space by the various interfaces on either sides of the P -type infinite, periodic minimal surface (IPMS) of zero mean average curvature (materialized by the green isosurface in Figures 9 and S8). The cyanobiphenyl-containing layers swollen by ionic metallacycles wrap this minimal surface. Simultaneously, the dendritic moieties are repelled on either along the edges and intersections at the corners, or along lines going through the centers of the faces and of the cube, and clustered into interwoven labyrinth-like domains. The inhomogeneities of the latter zones (e.g., shrinkage on edges and dilation on vertices) are modulated by the great flexibility and deformability of the dendritic cores. The fluid aliphatic continuums are intercalated between both these two types of disjointed domains, and delimited respectively by the interfaces with the mesogenic parts (blue isosurfaces in Figures 9 and S8) and by the somewhat shrunken interfaces with the dendritic cores (red interfaces in Figures 9 and S8). This multicontinuous model is therefore highly reminiscent of the lamellar structure of the P_n dendrimers, which shows the same sequence of strata from the minimal surface toward edges and vertices. A geometric link between both structures is found with the half-face diagonals, which in the model is normal to the successive segment strata (see below), and those lengths (~ 61 Å) are close to the layer spacing. A perfect coincidence was indeed not expected, due to several concomitant effects, among which the contribution of the metallacycles, the curvature of the interfaces and the related shrinking of the strata with the distance to the minimal surface.

The portion of the stratum covered by a single segment block, i.e., the area per segment, compensates to a certain extent the wedge shape of the entire encapsulated molecule. These

areas become then closer to the natural cross sections and reduce the interfaces between the various incompatible segments for an overall improved packing. The efficiency of the process can be quantified using surface foliations of the lattice volume,^{37,38} whereby the isosurfaces sharing the lattice in accordance with the segment volume fractions are assimilated into interfaces. For both molecules, this geometric modeling yields areas per segment³⁹ that decrease from ca. 235–240 and 345–350 Å², respectively, on the minimal surface, to 190–195 and 295–300 Å², at the interface with the aliphatic strata and finally to 120–125 Å² and 215–220 Å² at the interface with the dendritic part. The latter areas are in agreement with the expected overall cross-section of the dendritic branches (roughly 110 and 200 Å²), while the larger areas close to the minimal surface are compatible with the contribution of inserted ionic moieties. Remarkably, even the cross sections of aliphatic segments are approached at both interfaces, when taken into account the intermingling DOS chain ends.

The surface foliation model accounts for an almost ideal compensation of the cross section discrepancies and is so far consistent with all experimental data, unlike a few other reported systems, though of completely different nature.³⁶ For a clearer insight of the distribution of segregated zones in the cubic cell, sectional simulated sketches within most important crystallographic planes are represented for both complexes (Figure 10). The families of planes {100} and {200} contain the two labyrinths' directions and cut the third orthogonally. The strata crossed by the half-face diagonals remind the

lamellae of the pyrenyl-dendrimers (see above). The {111} plane cuts all three labyrinths' directions with the same angle. This plane might evolve toward a columnar lattice plane at higher swelling degrees, when edges resorb and superposed vertices merge to stratified columns. Instead of swelling mesogens, the shrinking of the dendritic part might yield a further original “mixed micellar-bicontinuous” mesophase, when edges stay wrapped by the aliphatic strata, while the dendritic fractions aggregate on the vertices.

The general design of these materials offers a wide range of possibilities to modulate the structures of the mesophases. Further deepening of these structures would require additional experimental information, such as more accurate volumes and shapes of segments, probably in combination with systematic variations of spacer and mesogen lengths. Such future developments would also be desirable owing to the original molecular architecture, different from mesogens connected to unequal aliphatic tails as previously described in the literature.

CONCLUSION

The syntheses of pyrenyl-functionalized poly(arylester) dendrimers with cyanobiphenyl end-groups and of a tetrานuclear arene ruthenium metallacycle $[\text{Ru}_4(p\text{-cymene})_4(\text{bpe})_2(\text{donq})_2]^{4+}$ isolated as a dodecyl sulfate salt are reported. The assembly of these two entities leads to supramolecular organometallic compounds. The dendrimers show a liquid-crystalline behavior which is identified as a multilayered smectic (LamSmA) phase, whereas the supramolecular assemblies self-organize into an intricate, multi-continuous $I\bar{m}\bar{3}m$ cubic phase. The wedge shape of the dodecylsulfate assemblies versus that formed with the triflate system is believed to be a key condition for the appearance of this mesophase, for which a structural model was proposed. Finally, because of the versatility of our system for which building-blocks are easily modified and interchanged, the perspectives for these supramolecular liquid-crystalline hybrids are huge.

ASSOCIATED CONTENT

Supporting Information

Synthesis and characterization of all new compounds. Elucidation of the mesophase from the diffractogram is described. This material is available free of charge via the Internet at <http://pubs.acs.org>.

AUTHOR INFORMATION

Corresponding Authors

bertrand.donnio@ipcms.unistra.fr
bruno.therrien@unistra.fr
robert.deschenaux@unistra.fr

Notes

The authors declare no competing financial interest.

ACKNOWLEDGMENTS

A generous loan of ruthenium chloride hydrate from Johnson Matthey Technology Centre is gratefully acknowledged. B.D. and B.H. are very grateful to Dr. Guillaume Weick (IPCMS) for his help regarding the IPMS mathematical calculations and to the CNRS for support. R.D. thanks the Swiss National Science Foundation (Grant No 200020–140298) for financial support.

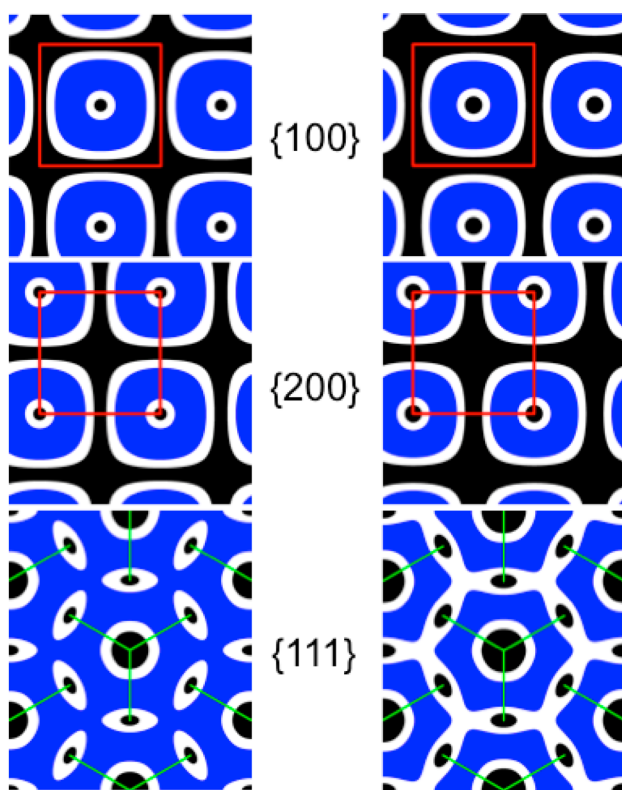


Figure 10. Simulated distribution of segregated zones in the cubic cell for complexes $[\text{P}_2 \subset 1][\text{DOS}]_4$ (left), and $[\text{P}_3 \subset 1][\text{DOS}]_4$ (right), within most important crystallographic families of planes (blue: mesogens + metallacycles sublayers; white: aliphatic strata; black: dendritic cores labyrinths; red frame: cubic lattice; green lines: edges to vertices from next plane).

■ REFERENCES

- (1) (a) Donnio, B.; Guillon, D.; Bruce, D. W.; Deschenaux, R. Metallomesogens. In *Comprehensive Coordination Chemistry II: From Biology to Nanotechnology*; McCleverty, J. A., Meyer, T. J., Eds.; Elsevier: Oxford, U.K., 2003; Vol. 7 (Fujita, M., Powell, A., Creutz, C., Eds.), pp 357–627. (b) Donnio, B.; Guillon, D.; Bruce, D. W.; Deschenaux, R. Metallomesogens. In *Comprehensive Organometallic Chemistry III: From Fundamentals to Applications*; Crabtree, R. H., Mingos, D. M. P., Eds.; Elsevier: Oxford, U.K., 2006; Vol. 12 (O'Hare, D., Ed.), pp 195–294. (c) Pucci, D.; Donnio, B. Metal-containing liquid crystals. In *Handbook of Liquid Crystals*; Goodby, J. W., Collings, P. J., Kato, T., Tschierske, C., Gleeson, H., Raynes, P., Eds.; Wiley-VCH: Weinheim, 2014; Vol. 5.
- (2) (a) Date, R. W.; Fernandez Iglesias, E.; Rowe, K. E.; Elliott, J. M.; Bruce, D. W. *Dalton Trans.* **2003**, 1914–1931. (b) Binnemans, K. *J. Mater. Chem.* **2009**, *19*, 448–453.
- (3) (a) Rao, N. V. S.; Choudhury, T. D.; Paul, M. K.; Francis, T. *Liq. Cryst.* **2009**, *36*, 409–423. (b) Prokhorov, A. M.; Santoro, A.; Williams, J. A. G.; Bruce, D. W. *Angew. Chem., Int. Ed.* **2012**, *51*, 95–98.
- (4) (a) Frein, S.; Auzias, M.; Sondenecker, A.; Vieille-Petit, L.; Guinchin, B.; Maringa, N.; Süss-Fink, G.; Barberá, J.; Deschenaux, R. *Chem. Mater.* **2008**, *20*, 1340–1343. (b) Santoro, A.; Wegzyn, M.; Whitwod, A. C.; Donnio, B.; Bruce, D. W. *J. Am. Chem. Soc.* **2010**, *132*, 10689–10691.
- (5) (a) Kim, D.-J.; Oh, N.-K.; Lee, M.; Choi, M.-G. *Mol. Cryst. Liq. Cryst.* **1996**, *280*, 129–134. (b) Massiot, P.; Impérator-Clerc, M.; Veber, M.; Deschenaux, R. *Chem. Mater.* **2005**, *17*, 1946–1951. (c) Matsuo, Y.; Muramatsu, A.; Kamikawa, Y.; Kato, T.; Nakamura, E. *J. Am. Chem. Soc.* **2006**, *128*, 9586–9587.
- (6) (a) El-ghayouri, A.; Douce, L.; Skoulios, A.; Ziessel, R. *Angew. Chem., Int. Ed.* **1998**, *37*, 2205–2208. (b) Ziessel, R.; Douce, L.; El-ghayouri, A.; Harriman, A.; Skoulios, A. *Angew. Chem., Int. Ed.* **2000**, *39*, 1489–1493.
- (7) (a) Barberá, J.; Elduque, A.; Giménez, R.; Lahoz, F. J.; López, J. A.; Oro, L. A.; Serrano, J. L. *Inorg. Chem.* **1998**, *37*, 2960–2967. (b) Kishimura, A.; Yamashita, T.; Yamaguchi, K.; Aida, T. *Nat. Mater.* **2005**, *4*, 546–549. (c) Frischmann, P. D.; Guieu, S.; Tabeshi, R.; MacLachlan, M. J. *J. Am. Chem. Soc.* **2010**, *132*, 7668–7675.
- (8) (a) Terazzi, E.; Bourgogne, C.; Welter, R.; Gallani, J.-L.; Guillon, D.; Rogez, G.; Donnio, B. *Angew. Chem., Int. Ed.* **2008**, *47*, 490–495. (b) Molard, Y.; Dorson, F.; Circu, V.; Roisnel, T.; Artzner, F.; Cordier, S. *Angew. Chem., Int. Ed.* **2010**, *49*, 3351–3355. (c) Mocanu, A. S.; Amela-Cortes, M.; Molard, Y.; Circu, V.; Cordier, S. *Chem. Commun.* **2011**, *47*, 2056–2058. (d) Terazzi, E.; Rogez, G.; Gallani, J.-L.; Donnio, B. *J. Am. Chem. Soc.* **2013**, *135*, 2708–2722.
- (9) Kadkin, O.; Galyametdinov, Y.; Rakhamatullin, A. *Mol. Cryst. Liq. Cryst.* **1999**, *332*, 2619–2628.
- (10) (a) Deschenaux, R.; Turpin, F.; Guillon, D. *Macromolecules* **1997**, *30*, 3759–3765. (b) Deschenaux, R.; Jauslin, I.; Scholten, U.; Turpin, F.; Guillon, D.; Heinrich, B. *Macromolecules* **1998**, *31*, 5647–5654. (c) Seredyuk, M.; Gaspar, A. B.; Ksenofontov, V.; Galyametdinov, Y.; Verdaguera, M.; Villain, F.; Gütl, P. *Inorg. Chem.* **2008**, *47*, 10232–10245. (d) Barberá, J.; Lantero, I.; Moyano, S.; Serrano, J. L.; Elduque, A.; Giménez, R. *Chem.—Eur. J.* **2010**, *16*, 14545–14553. (e) Seredyuk, M.; Gaspar, A. B.; Ksenofontov, V.; Galyametdinov, Y.; Verdaguera, M.; Villain, F.; Gütl, P. *Inorg. Chem.* **2010**, *49*, 10022–10031. (f) Dechambenoit, P.; Ferlay, S.; Donnio, B.; Guillon, D.; Hosseini, M. W. *Chem. Commun.* **2011**, *47*, 734–736.
- (11) (a) Camerel, F.; Strauch, P.; Antonietti, M.; Faul, C. F. J. *Chem.—Eur. J.* **2003**, *9*, 3764–3771. (b) Camerel, F.; Barberá, J.; Otsuki, J.; Tokimoto, T.; Shimazaki, Y.; Chen, L.-Y.; Liu, S.-H.; Lin, M.-S.; Wu, C.-C.; Ziessel, R. *Adv. Mater.* **2008**, *20*, 3462–3467. (c) Li, W.; Yin, S.; Wang, J.; Wu, L. *Chem. Mater.* **2008**, *20*, 514–522. (d) Molard, Y.; Ledneva, A.; Amela-Cortes, M.; Circu, V.; Naumov, N. G.; Mériaud, C.; Artzner, F.; Cordier, S. *Chem. Mater.* **2011**, *23*, 5122–5130. (e) Floquet, S.; Terazzi, E.; Hijazi, A.; Guénée, L.; Piguet, C.; Cadot, E. *New J. Chem.* **2012**, *36*, 865–868.
- (12) (a) Donnio, B.; Buathong, S.; Bury, I.; Guillon, D. *Chem. Soc. Rev.* **2007**, *36*, 1495–1513. (b) Rosen, B. M.; Wilson, C. J.; Wilson, D. A.; Peterca, M.; Imam, M. R.; Percec, V. *Chem. Rev.* **2009**, *109*, 6275–6540. (c) Donnio, B. *Inorg. Chim. Acta* **2014**, *409*, 53–67.
- (13) Baranoff, E. D.; Voignier, J.; Yasuda, T.; Heitz, V.; Sauvage, J.-P.; Kato, T. *Angew. Chem., Int. Ed.* **2007**, *46*, 4680–4683.
- (14) (a) Aprahamian, I.; Yasuda, T.; Ikeda, T.; Saha, S.; Ditchel, W. R.; Isoda, K.; Kato, T.; Stoddart, J. F. *Angew. Chem., Int. Ed.* **2007**, *46*, 4675–4679. (b) Kidowaki, M.; Nakajima, T.; Araki, J.; Inomata, A.; Ishibashi, H.; Ito, K. *Macromolecules* **2007**, *40*, 6859–6862. (c) Yasuda, T.; Tanabe, K.; Tsuji, T.; Coti, K. K.; Aprahamian, I.; Stoddart, J. F.; Kato, T. *Chem. Commun.* **2010**, *46*, 1224–1226. (d) Suhan, N. D.; Loeb, S. J.; Eichhorn, S. H. *J. Am. Chem. Soc.* **2013**, *135*, 400–408.
- (15) Terazzi, E.; Jensen, T. B.; Donnio, B.; Buchwalder, K.; Bourgogne, C.; Rogez, G.; Heinrich, B.; Gallani, J.-L.; Piguet, C. *Dalton Trans.* **2011**, *40*, 12028–12032.
- (16) (a) Lenoble, J.; Maringa, N.; Campidelli, S.; Donnio, B.; Guillon, D.; Deschenaux, R. *Org. Lett.* **2006**, *8*, 1851–1854. (b) Lenoble, J.; Campidelli, S.; Maringa, N.; Donnio, B.; Guillon, D.; Yevlampieva, N.; Deschenaux, R. *J. Am. Chem. Soc.* **2007**, *129*, 9941–9952. (c) Deschenaux, R.; Donnio, B.; Guillon, D. *New J. Chem.* **2007**, *31*, 1064–1073.
- (17) Barry, N. P. E.; Furrer, J.; Freudenberg, J.; Süss-Fink, G.; Therrien, B. *Eur. J. Inorg. Chem.* **2010**, 725–728.
- (18) (a) Neve, F. *Adv. Mater.* **1996**, *8*, 277–289. (b) Bruce, D. W. *Acc. Chem. Res.* **2000**, *33*, 831–840. (c) Binnemans, K. *Chem. Rev.* **2005**, *105*, 4148–4204. (d) Pucci, D. *Liq. Cryst.* **2011**, *38*, 1451–1465.
- (19) (a) Therrien, B. *Eur. J. Inorg. Chem.* **2009**, 2445–2453. (b) Barry, N. P. E.; Therrien, B. *Eur. J. Inorg. Chem.* **2009**, 4695–4700. (c) Barry, N. P. E.; Zava, O.; Dyson, P. J.; Therrien, B. *Chem.—Eur. J.* **2011**, *17*, 9669–9677. (d) Schmitt, F.; Freudenberg, J.; Barry, N. P. E.; Juillerat-Jeanneret, L.; Therrien, B. *J. Am. Chem. Soc.* **2012**, *134*, 754–757.
- (20) (a) Pitto-Barry, A.; Barry, N. P. E.; Zava, O.; Deschenaux, R.; Dyson, P. J.; Therrien, B. *Chem.—Eur. J.* **2011**, *17*, 1966–1971. (b) Pitto-Barry, A.; Barry, N. P. E.; Zava, O.; Deschenaux, R.; Therrien, B. *Chem.—Asian J.* **2011**, *6*, 1595–1603.
- (21) Moore, J. S.; Stupp, S. I. *Macromolecules* **1990**, *23*, 65–70.
- (22) Dardel, B.; Guillon, D.; Heinrich, B.; Deschenaux, R. *J. Mater. Chem.* **2001**, *11*, 2814–2831.
- (23) Garcí, A.; Martí, S.; Schürch, S.; Therrien, B. *RSC Adv.* **2014**, *4*, 8597–8604.
- (24) Barry, N. P. E.; Furrer, J.; Therrien, B. *Helv. Chim. Acta* **2010**, *93*, 1313–1328.
- (25) Campidelli, S.; Lenoble, J.; Barberá, J.; Paolucci, F.; Marcaccio, M.; Paolucci, D.; Deschenaux, R. *Macromolecules* **2005**, *38*, 7915–7925.
- (26) Marcos, M.; Giménez, R.; Serrano, J.-L.; Donnio, B.; Heinrich, B.; Guillon, D. *Chem.—Eur. J.* **2001**, *7*, 1006–1013.
- (27) Nagy, Z. T.; Heinrich, B.; Guillon, D.; Tomczyk, J.; Stumpe, J.; Donnio, B. *J. Mater. Chem.* **2012**, *22*, 18614–18622.
- (28) Guillon, D.; Skoulios, A. *Mol. Cryst. Liq. Cryst.* **1983**, *91*, 341–352.
- (29) (a) Hamley, I. W. *Angew. Chem., Int. Ed.* **2003**, *42*, 1692–1712. (b) Tschierske, C. *Annu. Rep. Prog. Chem., Sect. C: Phys. Chem.* **2001**, *97*, 191–267. (c) Lee, M.; Cho, B. K.; Zin, W. C. *Struct. Bonding (Berlin, Ger.)* **2008**, *128*, 63–98. (d) Tschierske, C. *Angew. Chem., Int. Ed.* **2013**, *52*, 8828–8878.
- (30) (a) Xu, B.; Swager, T. M. *J. Am. Chem. Soc.* **1993**, *115*, 1159–1160. (b) Swager, T. M.; Xu, B. *J. Inclusion Phenom. Mol. Recognit. Chem.* **1994**, *19*, 389–398. (c) Felder, D.; Heinrich, B.; Guillon, D.; Nicoud, J.-F.; Nierengarten, J.-F. *Chem.—Eur. J.* **2000**, *6*, 3501–3507.
- (31) (a) Balagurusamy, V. S. K.; Ungar, G.; Percec, V.; Johansson, G. *J. Am. Chem. Soc.* **1997**, *119*, 1539–1555. (b) Hudson, S. D.; Jung, H.-T.; Percec, V.; Cho, W.-D.; Johansson, G.; Ungar, G.; Balagurusamy, V. S. K. *Science* **1997**, *278*, 449–452. (c) Yeardley, D. J. P.; Ungar, G.; Percec, V.; Holerka, M. N.; Johansson, G. *J. Am. Chem. Soc.* **2000**, *122*, 1684–1689. (d) Duan, H.; Hudson, S. D.; Ungar, G.; Holerka, M. N.; Percec, V. *Chem.—Eur. J.* **2001**, *7*, 4134–4141. (e) Sun, H.-J.; Zhang, S.; Percec, V. *Chem. Soc. Rev.* **2015**, DOI: 10.1039/C4CS00249K.

(32) $0kl: k+l = 2n, hhl: l = 2n, h00: h = 2n$. *International Tables for Crystallography*, 4th ed.; Hahn, T., Ed.; Kluwer Academic: Dordrecht, The Netherlands, 1995; Vol. A, p 592.

(33) (a) Diele, S. *Curr. Opin. Colloid Interface Sci.* **2002**, *7*, 333–342.
(b) Kutsumizu, S. *Curr. Opin. Solid State Mater. Sci.* **2003**, *6*, 537–543.

(34) (a) Levelut, A.-M.; Clerc, M. *Liq. Cryst.* **1998**, *24*, 105–115.
(b) Impérator-Clerc, M. *Curr. Opin. Colloid Interface Sci.* **2005**, *9*, 370–376.

(35) La, Y.; Park, C.; Shin, T. J.; Joo, S. H.; Kang, S.; Kim, K. T. *Nat. Chem.* **2014**, *6*, 534–541.

(36) Zeng, X.; Ungar, G.; Impérator-Clerc, M. *Nat. Mater.* **2005**, *4*, 562–567.

(37) Fogden, A.; Lidin, S. *J. Chem. Soc., Faraday Trans.* **1994**, *90*, 3423–3431.

(38) The distribution of segregated domains in the cubic cell was analyzed using the following mathematical equation for the isosurfaces (from refs 34 and 37): $\cos(2\pi x) + \cos(2\pi y) + \cos(2\pi z) - \cos(2\pi x)\cos(2\pi y)\cos(2\pi z) = \beta$, where variables x , y and z refer to the unit cell normed to 1, and β defines the successive isosurfaces, starting from $\beta = 0$, for the approximation of the IPMS of type P , up to $|\beta| = 2$ on edges and vertices. The curvature regularly increases with $|\beta|$, while the isosurface area in the normed cell, A , simultaneously shrinks from 2.35 on IPMS to 0 on the edges. Isosurfaces β are hypothesized to coincide with domain boundaries when the volume fractions ($X_v/2$) separating them from the IPMS accord with the real volume of segments. The distribution of interfaces is therefore determined by these volume contributions and by the relation between β , X_v and A (Figures S9 and S10). The latter was obtained by numeric integration over cell volume and over membranes going through isosurfaces. The ratio of the isosurface area in the real cell a^2A and of the number of molecules per cell a^3/V_{mol} gives access to areas per segment that can be compared to natural cross-sections.

(39) Mesogens/aliphatic interfaces ($[P_2 \subset 1][DOS]_4$: $X_v \approx 0.31$, $|\beta| \approx 1.44$, $A = 1.92$; $[P_3 \subset 1][DOS]_4$: $X_v \approx 0.28$, $|\beta| \approx 1.30$, $A = 2.015$) and dendritic/aliphatic interfaces ($[P_2 \subset 1][DOS]_4$: $X_v \approx 0.44$, $|\beta| \approx 1.89$, $A = 1.21$; $[P_3 \subset 1][DOS]_4$: $X_v \approx 0.41$, $|\beta| \approx 1.80$, $A = 1.47$).